Nano Research

Open Access

Research Article

# Enhancing output performance of triboelectric nanogenerator by increasing charge storage capacity of electrodes

Congcong Hao, Zekun Wang, Mingzhe Cai, Shuaining Cheng, Zhongxin Wang, Cong Zhai, Juan Cui, Yongqiu Zheng ✉, and Chenyang Xue

*Key Laboratory of Instrumentation Science and Dynamic Measurement Ministry of Education, North University of China, Taiyuan 030051, China*

**Cite this article:** *Nano Research*, **2025**, *18*, 94907039. https://doi.org/10.26599/NR.2025.94907039

**ABSTRACT:** The practical application of rotating triboelectric nanogenerators is often limited by the wear of high-friction surface materials and low surface charge density. In addition to the charge pump replenishment strategy, suppressing charge decay is also crucial for increasing surface charge density. Here, we present a high performance rotary triboelectric nanogenerator (HPR-TENG) based on a coplanar charge pumping strategy and polyvinyl chloride (PVC) film. It has been demonstrated that applying PVC film to the surface of the storage electrode of the main TENG (M-TENG) significantly enhances the M-TENG's output performance. Furthermore, the HPR-TENG with three layers of PVC film pasted achieved the best output performance, with a peak-to-peak output voltage of 2828 V, a peak-to-peak output current of 327 μA and a charge transfer of 0.81 μC at 500 rpm. In addition, the output improvement effects of different materials are ranked. the TENG with 3 layers of PVC film pasted on it has a maximum output power of 748 mW at a load resistance of 4 × $10^6$ Ω. HPR-TENG's output performance remains consistent after 100,000 cycles, which shows excellent stability. The excellent electrical performance of the HPR-TENG can be used as the energy supply for the tip high-voltage breakdown sensor system, which can achieve 14 breakdowns in 10 s. Due to its extraordinary electrical performance, HPR-TENG can not only serve as an energy supply for cutting-edge high-voltage breakdown sensor systems, but also has the potential to serve as an energy supply for high-pressure sterilization, high-pressure vacuum and water electrolysis.

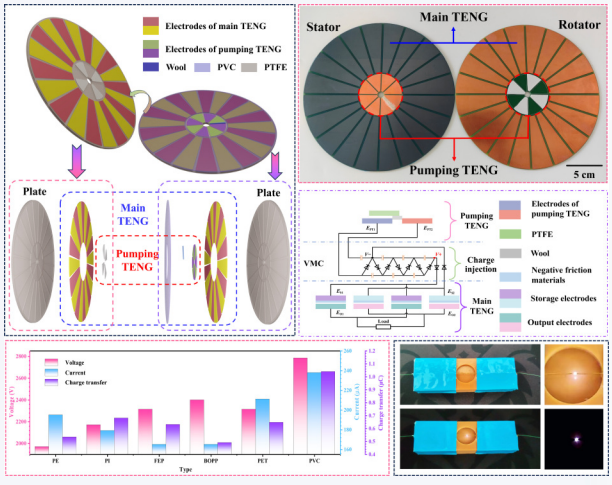


**KEYWORDS:** triboelectric nanogenerator, coplanar charge pump, enhancing charge density, suppressing charge decay, polyvinyl chloride (PVC) film

## 1 Introduction

In the era of the Internet of Things (IoT) and artificial intelligence, distributed and low-power sensors are increasingly being used to collect information [1–3]. Most sensor nodes in IoT are powered by batteries, which have limited lifetimes and can cause environmental pollution [4]. Therefore, researchers are exploring sustainable and green energy sources, such as solar and wind energy, as supplements or alternatives. Triboelectric nanogenerators (TENGs), based on contact electrification and electrostatic induction, provide a promising approach as an alternative [4–6]. Since the invention of TENGs by Wang et al. in 2012 [7], TENGs have become a focal point of research due to their enormous potential for next-generation energy solutions [5, 8–10]. TENGs offer advantages such as low cost, maintenance-free operation, diverse material selection, flexible structures and environmental friendliness. TENGs have potential applications in self-powered sensing and high-voltage power supply and have made significant progress in these areas.

However, TENGs still face some challenges, such as low surface charge density [11, 12] and damage forces caused by contact electrification and surface friction. To improve the output performance of TENGs, previous studies have mainly focused on structural design [13–16], material optimization [17], surface

**Received:** August 24, 2024; **Revised:** September 13, 2024
**Accepted:** September 18, 2024

✉Address correspondence to zhengyongqiu@nuc.edu.cn

modification [18, 19], and environmental control [20]. By encapsulating in vacuum, Wang et al. [21] achieved an ultras-high charge density of 1003 μC·m$^{-2}$, but this not only posed significant challenges to device manufacturing but also deviated from practical applications. In recent years, emerging contact separation charge pump technologies [12, 22–24] has been proven to effectively break through the bottleneck of enhancing charge density. It can rapidly accumulate surface charge density to saturation and maintain it in a high charge density state, thereby improving output performance. Xu et al. [24] first used a charge pump to increase the charge density to 1020 μC·m$^{-2}$ in 2018. In 2020, Wang et al. [25] designed a contact separation charge pump that increased the charge density to 1850 μC·m$^{-2}$. Although these works have improved output, the problem of surface damage caused by friction still exists, which greatly limits the application of TENG. The non-contact mode TENG has durability due to its zero-friction loss [26]. Lin et al. [27] fabricated a soft contact TENG with high durability, but it has a low surface charge density of 10 μC·m$^{-2}$. Achieving high output while possessing the high durability of TENG remains a challenge. Lv et al. [22] proposed a coplanar charge pump soft contact TENG that combines high output performance and durability, with a charge density of up to 74.62 μC·m$^{-2}$. However, its frictional contact area is relatively large and the charge density still needs to be improved. In addition, there are currently few reports on how to reduce charge dissipation and maintain it in a high charge density state.

In this work, a high performance rotary TENG (HPR-TENG) based on a coplanar charge pumping strategy and polyvinyl chloride (PVC) film is developed. It has been proved by tests that pasting PVC film on the surface of the storage electrode of the main TENG (M-TENG) can enhance the output performance of the M-TENG more effectively. Pasting PVC film on the surface of the storage electrode not only raises the electrode storage threshold, but also acts as an insulator. The coplanar design of the pumping TENG (P-TENG) and M-TENG of the HPR-TENG greatly reduces the complexity of structural design. The P-TENG uses a wool-based self-compensating power strategy that greatly improves output performance. The HPR-TENG makes soft contact with just wool during rotation, greatly reducing frictional resistance. Moreover, pasting different friction materials has different effects on the charge storage capacity enhancement of the electrodes. The HPR-TENG with three layers of PVC film pasted on it achieved the best output performance, with a peak-to-peak output voltage of 2828 V, a peak-to-peak output current of 327 μA and a charge transfer of 0.81 μC at 500 rpm. Also, the lifting effects of different materials are ranked. the TENG with 3 layers of PVC film pasted on it has a maximum output power of 748 mW at a load resistance of 4 × 10$^6$ Ω. HPR-TENG's output performance remains consistent after 100,000 cycles, which shows excellent stability. The excellent electrical performance of the HPR-TENG can be used as the energy supply for the tip high-voltage breakdown sensor system, which can achieve 14 breakdowns in 10 s. Due to its extraordinary electrical performance, HPR-TENG can not only serve as an energy supply for cutting-edge high-voltage breakdown sensor systems, but also has the potential to serve as an energy supply for high-pressure sterilization, high-pressure vacuum and water electrolysis.

## 2 Results and discussion

### 2.1 Structural design and working principle

The HPR-TENG is uniquely designed with only the wool part in contact, significantly reducing friction resistance during operation. Figure 1(a) depicts the fundamental structure of the HPR-TENG, which comprises upper and lower pole plates. Each pole plate is divided into an inner central region and an outer annular region. The inner central region functions as a P-TENG, while the outer annular region serves as an M-TENG. The upper pole plate consists of the plate, electrodes and polytetrafluoroethylene (PTFE), while the lower pole plate includes PVC, wool, electrodes and a plate. Notably, the coplanar design of the P-TENG and M-TENG ensures synchronized rotation, simplifying the overall structure. On the upper pole plate, PTFE, as the negative friction material for P-TENG, is affixed at equal intervals within the inner central region. The outer annular region is subdivided into 20 equal sections, each containing output electrodes that are electrically connected by color. Conversely, the lower pole plate's inner central region contains P-TENG output electrodes spaced equally in eight small sections, with regions of the same color electrically connected. Wool is placed between the electrodes as a supplementary material for P-TENG. The outer annular region is similarly divided into 20 sections, all containing electrodes, but with PVC material applied to the surface, enhancing the HPR-TENG's output performance and insulation. The principle of PVC material to enhance the performance of HPR-TENG is demonstrated in Fig. S1 in the Electronic Supplementary Material (ESM). Figure 1(b) provides a physical illustration of the HPR-TENG, showing the stator (lower pole plate) on the left and the rotator (upper pole plate) on the right. The integration of electrodes and the plate into printed circuit boards (PCBs) significantly enhances the stability of the HPR-TENG's output and reduces production complexity. The advantages of HPR-TENG over other conventional rotating TENG structures are demonstrated in Note S1 in the ESM.

The basic working principle of HPR-TENG is self-compensating non-contact electrostatic induction, which simply means that HPR-TENG is able to improve its output performance by means of supplementary electric measures. Figure 1(c) shows a general schematic of the working principle. P-TENG works on the principle of self-supplementary electrostatic induction. In detail, the friction between the wool and the PTFE causes a negative charge to build up on the surface of the PTFE which does not dissipate easily. The PTFE then undergoes electrostatic induction with the electrodes, causing the electrodes to generate electrical energy output. The charge injection process is achieved by a voltage multiplication circuit (VMC). The workings of the VMC are shown in Note S2 in the ESM. Specifically, the electrical energy generated by the P-TENG is injected into the VMC and then the VMC steadily injects the electrical energy into the storage electrodes ($E_S$) of the M-TENG. M-TENG also works on the principle of non-contact electrostatic induction. The $E_S$ are charged by the VMC, which creates an extremely high charge density on the surface of the electrodes. In the electrostatic induction with the output electrode ($E_O$), a high-performance output is generated.

In order to understand the working principle of HPR-TENG more clearly, Figs. 1(d) and 1(e) explain the working principle of P-TENG and M-TENG in detail. In Fig. 1(d), P-TENG's friction material PTFE ($P_{(n)}$) fills the surface with a negative charge after electrostatic induction with wool. The advantages of attaching wool are demonstrated for the Note S3 in the ESM. In the process of states II to III, the positive charge in the output electrodes of P-TENG ($E_{PT(n)}$) is transferred to $E_{PT(n+1)}$ to generate electrical energy. In states IV to I, the positive charge moves from $E_{PT(n+1)}$ to $E_{PT(n)}$,

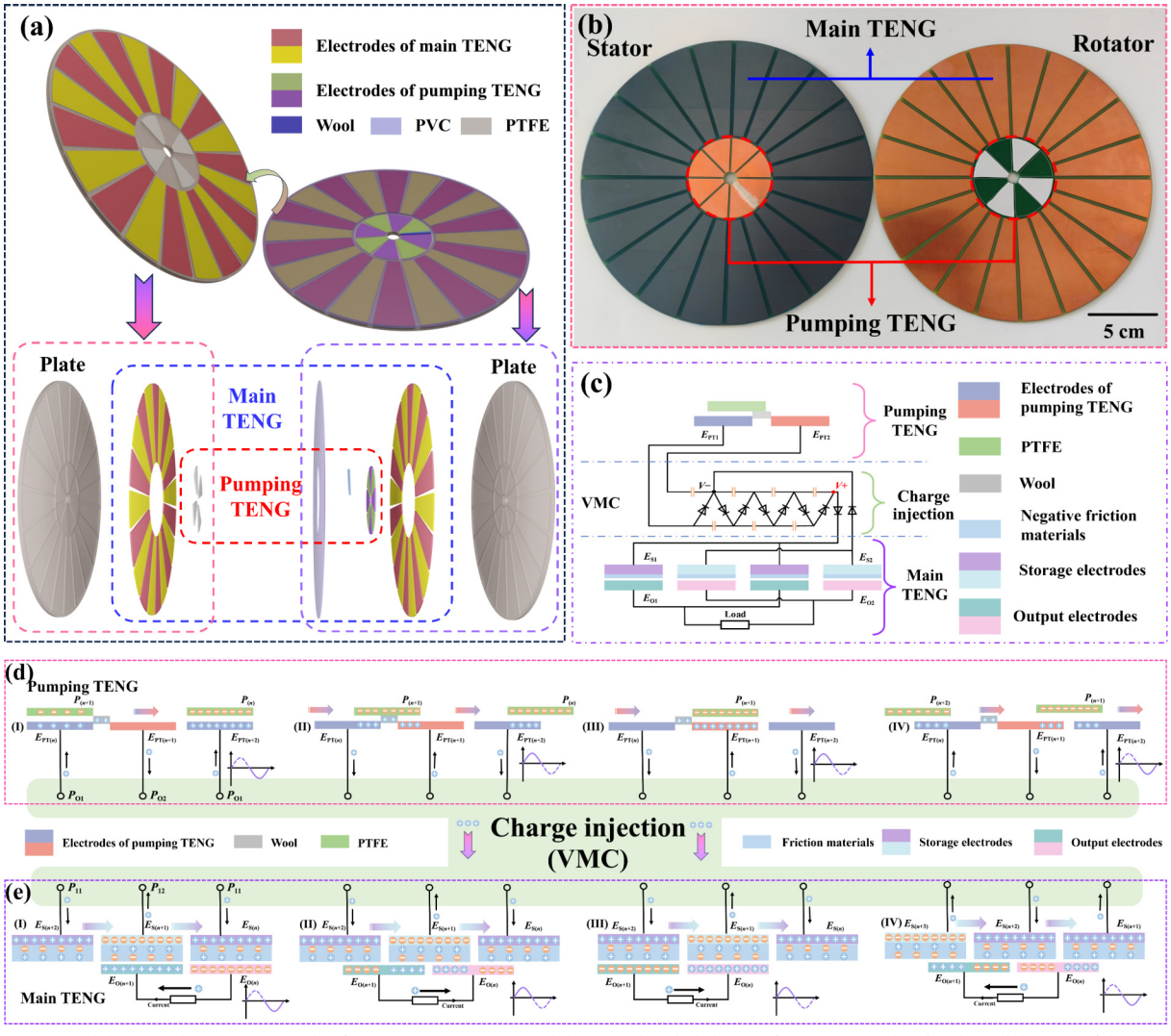


**Figure 1** Structural design and working principle of HPR-TENG. (a) Structural design and exploded view of HPR-TENG. (b) The physical drawing of the HPR-TENG. (c) The general schematic of the working principle. The working principle of (d) P-TENG and (e) M-TENG in detail.

producing the opposite charge transfer as in states II and III. Assuming that the transfer of positive charge from $E_{PT(n)}$ to $E_{PT(n+1)}$ is a positive current, the direction of the current generated by the process from states II to III is positive and the direction of the current generated by states IV to I is negative. Figure 1(e) shows in detail how M-TENG works. In state I, neighboring storage electrodes ($E_{S(n)}$) are stably injected with charges of different polarities by the VMC. Extremely high charge densities are formed on the surface of $E_{S(n)}$, but the surface charge density of the electrode is subject to a certain threshold, which limits the output performance of M-TENG to a certain extent. In order to enhance the $E_{S(n)}$ charge storage threshold, attaching the friction material to the surface of the storage electrode will provide an additional charge storage space, which in turn will enhance the charge storage capacity of the $E_{S(n)}$ as a whole. Specifically, the friction material affixed to the $E_{S(n)}$ surface stores the charge above the threshold. During the process from states II to III, the positive charge in the output electrode $E_{O(n+1)}$ moves into $E_{O(n)}$ to generate electrical energy. Since the polarity of $E_{S(n)}$ do not change, the $E_{O(n)}$ reverses its polarity. For example, $E_{O(n+1)}$ filled with a positive charge is now filled with a negative charge. The polarity of $E_{O(n+1)}$ is reversed so that M-TENG produces a double output. During the process from states IV to I, the positive charge is transferred from $E_{O(n)}$ into $E_{O(n+1)}$, which eventually completes the polarity reversal of the electrode. Assuming that the transfer of positive charge from $E_{O(n+1)}$ to $E_{O(n)}$ is a positive current, the currents generated by states II to III are positive and the currents generated by states IV and I are negative. Therefore, the electrical energy generated by P-TENG is injected into M-TENG via VMC to enhance the output performance of M-TENG is proved to be feasible in principle.

## 2.2 Discussion of complementary strategies

The performance of P-TENG as a source of energy input to the HPR-TENG has a great impact on the output performance of the HPR-TENG. To investigate the output performance of P-TENG, it is placed in a test environment with different rotational speeds. Figures 2(a) and 2(b) show the voltage and current results for P-TENG in different rpm environments, respectively. From Fig. 2(a), it can be visualized that the output voltage of the P-TENG roughly tends to increase as the rpm increases. More detailed data is the P-TENG's peak output voltage of 387.95 V at 500 rpm. A detailed explanation of this phenomenon is that the charge on the PTFE

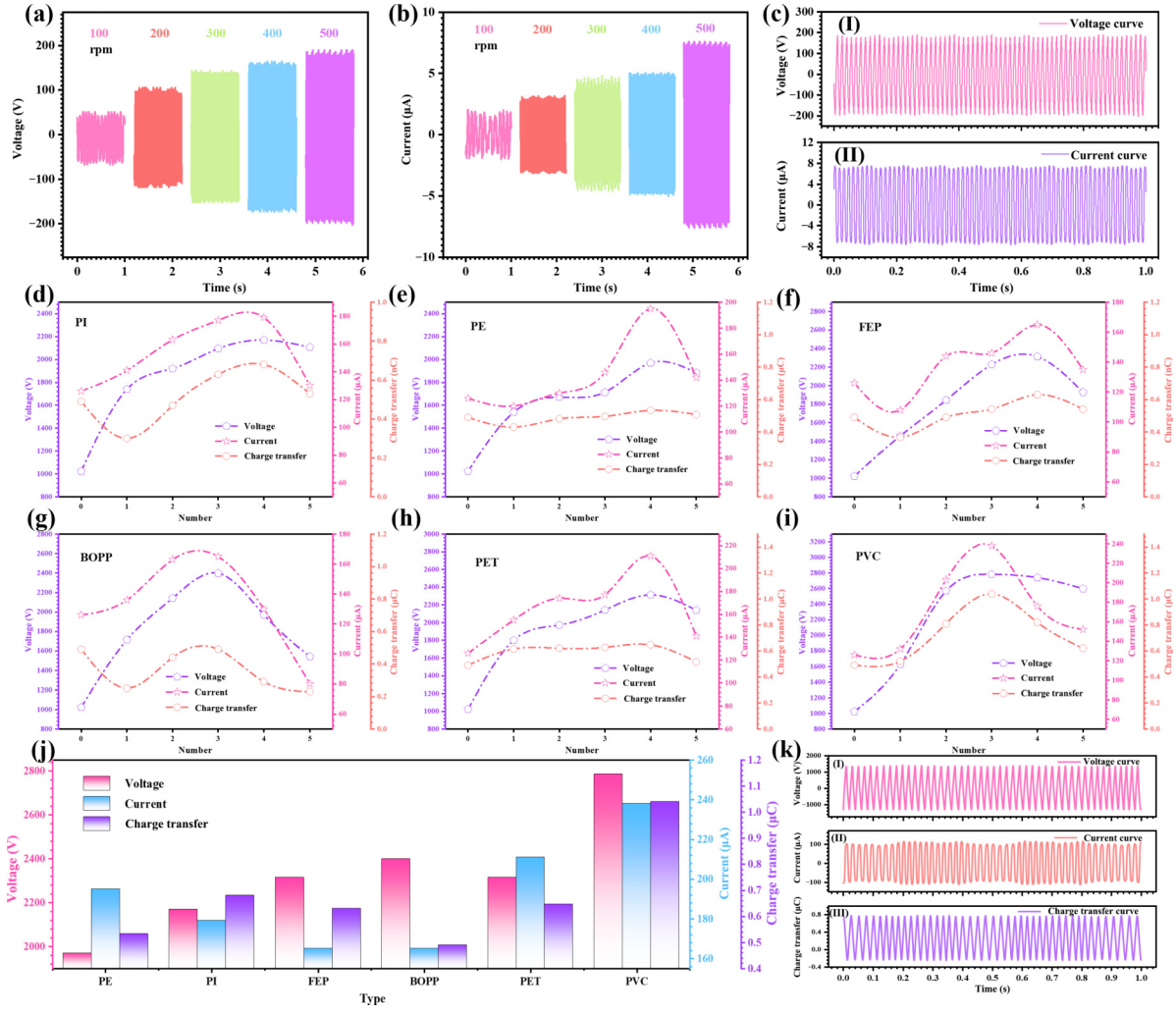


**Figure 2** P-TENG performance testing and friction material selection. The (a) voltage and (b) current results for P-TENG in different rpm environments, respectively. (c) The detailed curves of voltage and current for P-TENG in a test environment at an rpm of 500. The effect of friction materials (d) PI, (e) PE, (f) FEP, (g) BOPP, (h) PET and (i) PVC on the enhancement of electrode charge storage capacity, respectively. (j) The optimal lifting effect of different friction materials. (k) The optimal enhancement of the HPR-TENG output performance by the PVC film in detail.

surface of the P-TENG fades away during operation. As the rpm increases, the PTFE surface charge is rapidly supplemented. However, the P-TENG's output voltage does not increase indefinitely with increasing rpm, this is because increasing rpm simply brings the output performance closer to saturation. The magnitude of voltage saturation is determined by its own structure (the available area of the friction material). As a result, the output voltage of P-TENG increases as the rpm increases, with a gradual flattening out of the increasing trend and eventual saturation. It can be visualized from Fig. 2(b) that the output current of the P-TENG keeps increasing as the rpm increases. At an rpm of 500, P-TENG's output current peaks at 15.22 μA. The reason for this whole phenomenon is that the effect of the increase in rpm is an increase in frequency (decrease in cycle time), resulting in a decrease in the time for each charge transfer process. However, the total amount of charge transfer is constant and as the cycle time decreases, this ultimately leads to an increase in output. Therefore, the output current of P-TENG will continue to increase as the rpm increases. Figure 2(c) shows the detailed curves of voltage and current for P-TENG in a test environment at an rpm of 500. Where, Fig. 2(c)(I) depicts the voltage curve and Fig. 2(c)(II) shows the current curve.

Different friction materials exhibit varying degrees of enhancement on the charge storage capacity of the M-TENG. To investigate the effects of different friction materials and layer numbers on this enhancement, tests are conducted at an rpm of 150. The experimental results, shown in Figs. 2(d)–2(i), illustrate the impact of polyimide (PI), polyethylene (PE), fluorinated ethylene propylene (FEP), biaxially oriented polypropylene (BOPP), PE terephthalate (PET) and PVC on the electrode charge storage capacity. It is evident that all friction materials enhance charge storage capacity. Figure 2(d) highlights the effect of PI on the electrode storage capacity, with the optimal performance observed at four layers of PI material (0.06 mm thickness). The output voltage, current and charge transfer of M-TENG are 1970 V, 195 μA and 0.53 μC, respectively. Under the same test conditions, the friction material PE also shows the best output performance of M-TENG when 4 layers are pasted. The specific data are 2170 V, 179 μA, 0.68 μC (as shown in Fig. 2(e)). Similarly, the friction material FEP has the best output performance of M-TENG when 4 layers are pasted. The specific data are 2314 V, 165 μA and 0.63 μC (as shown in Fig. 2(f)). The friction material BOPP also has the best output performance of M-TENG when 4 layers are pasted.

The specific data are 2399 V, 165 μA and 0.49 μC (as shown in Fig. 2(g)). The friction material PET also has the best output performance of M-TENG when 4 layers are pasted. The specific data are 2314 V, 211 μA, 0.65 μC (as shown in Fig. 2(h)). The friction material PVC has the best output performance of main HPR-TENG when 3 layers are pasted. The specific data are 2785 V, 238 μA, 1.04 μC (as shown in Fig. 2(i)). Among the six tested materials, PVC emerged as the best performing friction material. As the number of layers increased, the M-TENG's output performance initially rose before declining. This is because additional friction material layers enhance the charge storage capacity of the M-TENG, significantly boosting output. However, when too many layers are applied, they impede the electrostatic induction process, thereby reducing output performance. Consequently, the M-TENG's storage electrodes achieve optimal performance with three layers of PVC friction material. A ranking of the friction materials' effectiveness in enhancing charge storage capacity is established, as illustrated in Fig. 2(j). The order, from highest to lowest enhancement, is: PVC, PET, BOPP, FEP, PI and PE. Figure 2(k) provides a detailed view of the optimal enhancement of HPR-TENG output performance by the PVC film. Fig. 2(k)(I) depicts the voltage curve, Fig. 2(k)(II) shows the current curve and Fig. 2(k)(III) presents the charge transfer curve.

### 2.3 Performance testing and result analysis of HPR-TENG

To study the effect of different rotational speeds on the output performance of M-TENG, M-TENG with 3 layers of PVC friction material pasted on it is selected for performance testing at different rpms. The voltage output curves of M-TENG at different speeds are shown in Fig. 3(a). It can be observed intuitively that at speeds of 100 and 200 rpm, the output voltage phases are roughly the same. At speeds of 300, 400 and 500 rpm, the output voltage is essentially the same. However, the difference in output voltage is not significant. This is because the output voltage is determined by the actual area of the friction material, which may vary a little due to differences in rpm (external test conditions). The peak output voltage of M-TENG at 500 rpm is 2828 V. Figure 3(b) shows the output current curves of M-TENG at different rpm. The output current curve shows a clear increasing trend as the speed increases. M-TENG has a peak output current of 327 μA at a test condition of 500 rpm. This is because as the rotational speed increases, it causes the frequency to increase (cycle time decreases). However, the amount of charge transfer completed within the cycle remains constant, which means that the charge transfer needs to be completed in a shorter amount of time. As a result, the output current of the M-TENG increases as the rpm increases. Figure 3(c) illustrates the charge transfer curves of M-TENG at different rpms.

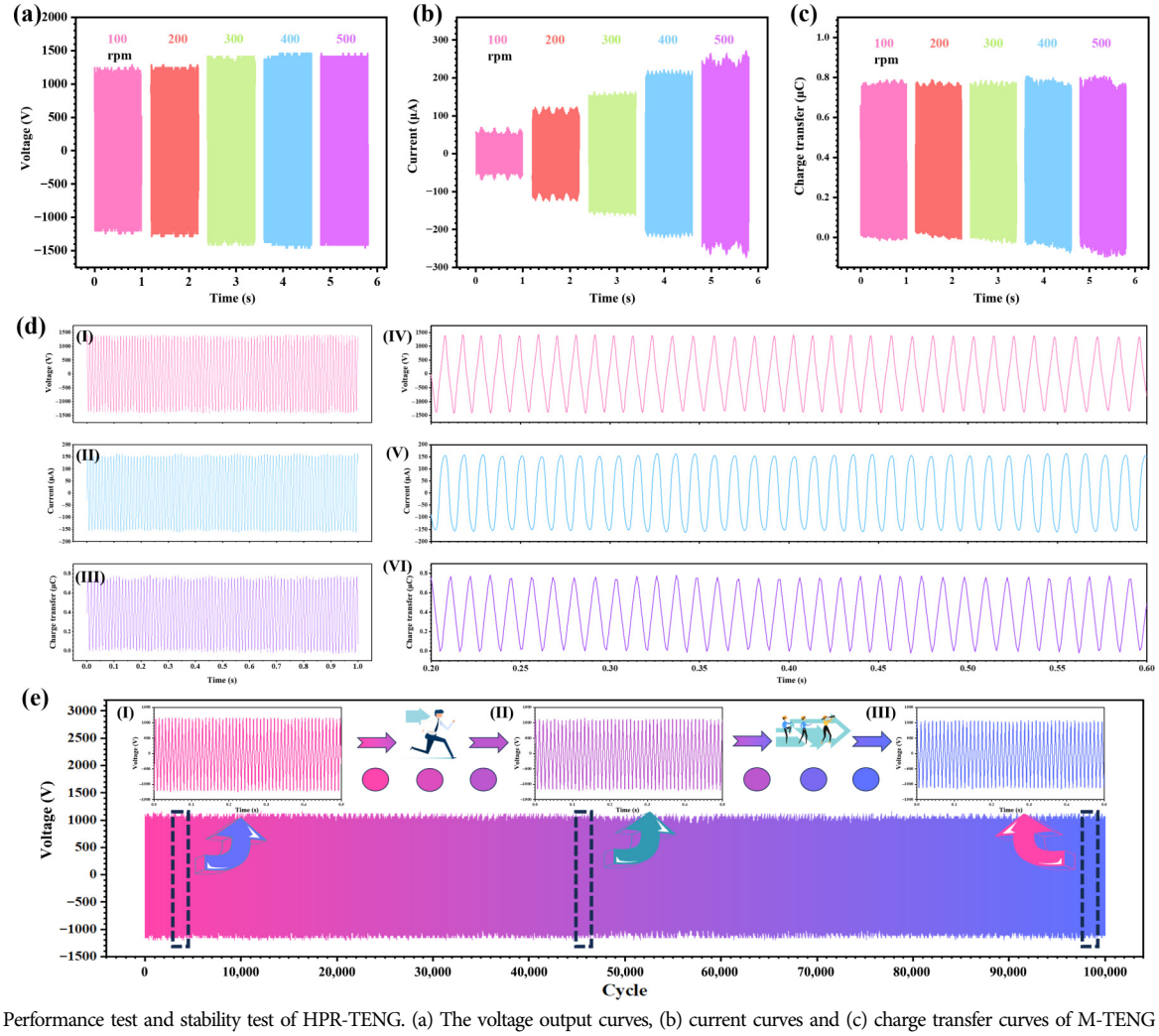


**Figure 3** Performance test and stability test of HPR-TENG. (a) The voltage output curves, (b) current curves and (c) charge transfer curves of M-TENG at different speeds. (d) The output voltage, current and charge transfer curves of the M-TENG at an rpm of 500. (e) The HPR-TENG after completing 100,000 operating cycles.

It can be intuitively seen that the output charge transfer of M-TENG is essentially the same at different rpms. At a rotational speed of 500, the charge transfer of M-TENG is 0.81 μC. This is due to the fact that the amount of charge transfer is determined by the effective area of the friction material and increasing the rpm only increases the speed of charge flow without affecting the total amount of charge transfer. Therefore, the amount of charge transfer in M-TENG does not change significantly as the rotational speed increases. For a more intuitive understanding of the output performance of the M-TENG, Fig. 3(d) shows the output voltage, current and charge transfer curves of the M-TENG at an rpm of 500. Figures 3(d)(I)–3(d)(III) show the thumbnail diagrams of output voltage, current and charge transfer, respectively and Figs. 3(d)(IV)–3(d)(VI) show the detailed diagrams of output voltage, current and charge transfer, respectively.

Stability is a key focus in HPR-TENG research. To test device stability, Fig. 3(e) presents data from the HPR-TENG after completing 100,000 operating cycles. Figures 3(e)(I)–3(e)(III) display some of the initial, intermediate and final work cycles, respectively. It is clear that the HPR-TENG maintains consistent performance during continuous operation, highlighting its structural stability. Consequently, the HPR-TENG not only delivers excellent output performance but also demonstrates remarkable stability.

### 2.4 Applications

The HPR-TENG should not only have excellent output performance, but also excellent applications. To test the application of HPR-TENG, we test the capability of charging capacity. After passing the output energy of the HPR-TENG through the rectifier bridge, it charges capacitors of different capacities with sizes of 1, 10, 100, 220, 330 and 470 μF. The results of charging curves for different capacitors are shown in Fig. 4(a). Wherein the inset in Fig. 4(a) is an enlarged area of a portion of the region. It can be visualized that charging is extremely fast for small capacity capacitors and relatively slow for large capacity capacitors. Detailed data demonstrates that it takes no more than 0.5 s to charge 1 and 10 μF capacitors to 5 V. A 100 μF capacitor takes 3.5 s to charge to 5 V, a 220 μF capacitor takes 7 s and relatively large capacitors take more time, 19.5 s for a 330 μF capacitor and 30 s for a 470 μF capacitor. As you can see, HPR-TENG demonstrates excellent application with its own excellent output performance.

Exploring the impedance of HPR-TENG allows for better applications. We matched the impedance of the HPR-TENG by using different resistors. The impedance will vary with different amounts of PVC film applied. Figs. 4(b)–4(f) show the HPR-TENG output power and voltage curves for pasting different amounts of PVC films. The experimental results demonstrate that the HPR-TENG with a layer of PVC film pasted on it achieves the maximum output power of 108 mW at a load resistance of $1 \times 10^7$ Ω. Similarly, the HPR-TENG with two layers of PVC film pasted on it has a maximum output power of 256 mW at $1 \times 10^7$ Ω. However, the HPR-TENG with 3 layers of PVC film pasted on it has a maximum output power of 748 mW at a load resistance of $4 \times 10^6$ Ω. The HPR-TENG with four layers of PVC film pasted on it reaches its maximum output power of 382 mW at a load resistance of $8 \times 10^6$ Ω. Moreover, the HPR-TENG with five layers of PVC film pasted on it reaches the maximum output power of 62 mW at a load resistance of $1 \times 10^7$ Ω. Therefore, the HPR-TENG with three layers of PVC film pasted on it is the maximum power output, which is 748 mW. The formula for calculating HPR-TENG peak power is shown in Note S4 in the ESM.

Tip high-voltage breakdown sensor system have been proven to be used for the detection of inert gas composition, concentration, humidity and other parameters [28–30]. The working principle of needle tip high voltage breakdown is shown in Note S5 in the ESM. Moreover, tip high-voltage breakdown has also been shown to be used to enhance the output performance of HPR-TENG. However, a large potential difference is required for tip high-voltage breakdown to occur. However, a large potential difference is required for pinpoint high voltage breakdown to occur. HPR-TENG has excellent output performance and can provide sufficient potential difference to the tip. Figure 4(g) shows the schematic diagram of the HPR-TENG for a tip high-voltage breakdown sensor system. The electrical energy generated by the HPR-TENG delivers a large number of charges of different polarities to each end of the tip through the VMC. Causes a high potential difference between the two tips of the needles, which eventually breaks through the air. Figure 4(h) shows the state of the tip of the needle when it is not breakdown and when it is breakdown, respectively. In order to understand more about the tip high-voltage breakdown when it occurs, information about the current and charge transfer at the tip over a period of 10 s is collected. Figure 4(i) shows the current information during the tip high-voltage breakdown of the tip. It can be seen that there are 14 breakdowns in 10 s with current up to about 30 mA. Figure 4(j) shows in detail the current profile during a tip high-voltage breakdown and it can be found that the tip high-voltage breakdown takes only 1 ms to occur. Figure 4(k) illustrates the charge transfer curve for a tip high-voltage breakdown and Fig. 4(l) details the charge transfer curve for one of the tip high-voltage breakdowns. Therefore, the HPR-TENG can be used as an excellent energy supply for tip high-pressure sensor system.

## 3 Conclusion

We have developed a HPR-TENG based on coplanar charge pumping strategy and suppression of charge decay. By pasting PVC film on the surface of the storage electrode of M-TENG, the storage threshold of the electrode can be increased, thereby more effectively improving the output performance of M-TENG. HPR-TENG comes into soft contact with wool during rotation, greatly reducing frictional resistance. The coplanar design of P-TENG and M-TENG in HPR-TENG greatly reduces the complexity of structural design. P-TENG adopts a self-compensating power supply strategy based on wool, greatly improving output performance. The enhancement effect of pasting different friction materials on the electrode charge storage capacity has been verified. Among them, HPR-TENG with three layers of PVC film pasted has the best output performance, with the output voltage of 2828 V, output current of 327 μA and the charge transfer amount of 0.81 μC at 500 rpm. The HPR-TENG with 3 layers of PVC film has a maximum output power of 748 mW when the load resistance is $4 \times 10^6$ Ω. The output performance of HPR-TENG remains stable after 100,000 cycles, demonstrating excellent stability. HPR-TENG has excellent electrical performance and can serve as an energy source for tip high-voltage breakdown sensor system, achieving 14 breakdowns within 10 s. HPR-TENG has the potential to serve as an energy supply for high-pressure sterilization, high-pressure vacuum and water electrolysis.

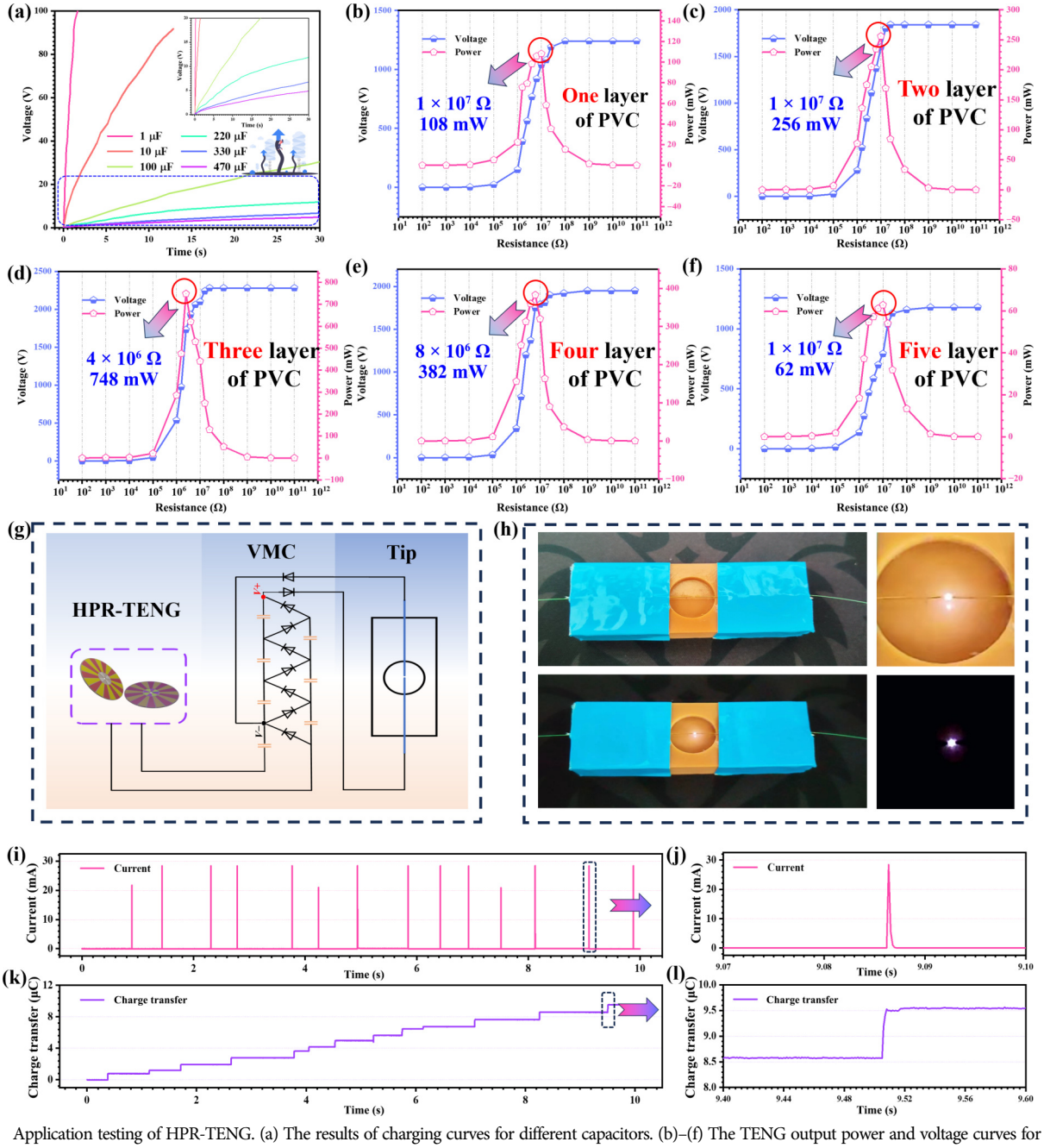


**Figure 4** Application testing of HPR-TENG. (a) The results of charging curves for different capacitors. (b)–(f) The TENG output power and voltage curves for pasting different amounts of PVC films. (g) The schematic diagram of the HPR-TENG for a tip high-voltage breakdown sensor system. (h) The state of the tip of the needle when it is not breakdown and when it is breakdown, respectively. (i) The current information during the tip high-voltage breakdown of the tip. (j) The current profile during a tip high-voltage breakdown in detail. (k) The charge transfer curve for a tip high-voltage breakdown. (l) The charge transfer curve for one of the tip high-voltage breakdowns in detail.

## 4 Experimental section

### 4.1 Design and fabrication of HPR-TENG

The rotor and stator were fabricated by attaching a copper layer of friction material to the surface using the PCB method. The design of the rotor and stator had a radius of 10 cm and the area was divided into a central area and an outer circle area. Among them, the radius of the central area was 3 cm. Friction materials PTFE, PVC, PET, BOPP, FEP, PI, PE and wool were purchased commercially.

### 4.2 Characterizations and measurements

The short-circuit current, amount of charge transfer and internal resistance of HPR-TENG were measured with an electrostatic meter (Keithley 6514) and the open-circuit voltage was measured with an oscilloscope (DS7054 500 MHz 10 GSa/s RIGOL) and a high-voltage probe (P5100A with an equivalent impedance of 40 MΩ Tektronix).

### 4.3 Statistical analysis

Statistics were performed using the software Origin (Origin lab Corporation, Northampton, MA, USA).

**Electronic Supplementary Material**: Supplementary material (further explain the working principle of HPR-TENG) is available in the online version of this article at https://doi.org/10.26599/NR.2025.94907039.

## Data availability

All data needed to support the conclusions in the paper are presented in the manuscript and the Electronic Supplementary Material. Additional data related to this paper may be requested from the corresponding author upon request.

## Acknowledgements

We gratefully acknowledge support from the Natural Science Foundation for Young Scientists of Shanxi Province (No. 202203021212127) and the Innovative Research Group Project of National Natural Science Foundation of China (No. 51821003).

## Declaration of competing interest

All the contributing authors report no conflict of interests in this work.

## Author contribution statement

C. C. H.: Conceptualization, data curation, funding acquisition, writing – original draft, writing – review & editing. Z. K. W.: Data curation, writing – original draft, writing – review & editing, visualization. M. Z. C.: Supervision, investigation, visualization. S. N. C.: Data curation, visualization, conceptualization. Z. X. W.: Data curation, visualization, conceptualization. C. Z.: Investigation, methodology, supervision. J. C.: Investigation, methodology, supervision. Y. Q. Z.: Funding acquisition, investigation, writing – review & editing. C. Y. X.: Conceptualization, methodology, project administration, writing – review & editing. All authors have approved the final manuscript.

## Use of AI statement

None.

## References

[1] Wang, Z. L. Triboelectric nanogenerator (TENG)-sparking an energy and sensor revolution. *Adv. Energy Mater.* **2020**, *10*, 2000137.

[2] Shi, Q. F.; Dong, B. W.; He, T. Y. Y.; Sun, Z. D.; Zhu, J. X.; Zhang, Z.; Lee, C. Progress in wearable electronics/photonics-moving toward the era of artificial intelligence and internet of things. *InfoMat* **2020**, *2*, 1131–1162.

[3] Sengupta, D.; Romano, J.; Kottapalli, A. G. P. Electrospun bundled carbon nanofibers for skin-inspired tactile sensing, proprioception and gesture tracking applications. *npj Flex. Electron.* **2021**, *5*, 29.

[4] Bai, Y.; Xu, L.; Lin, S. Q.; Luo, J. J.; Qin, H. F.; Han, K.; Wang, Z. L. Charge pumping strategy for rotation and sliding type triboelectric nanogenerators. *Adv. Energy Mater.* **2020**, *10*, 2000605.

[5] Wu, C. S.; Wang, A. C.; Ding, W. B.; Guo, H. Y.; Wang, Z. L. Triboelectric nanogenerator: A foundation of the energy for the new era. *Adv. Energy Mater.* **2019**, *9*, 1802906.

[6] Wang, Z. L. On the first principle theory of nanogenerators from Maxwell's equations. *Nano Energy* **2020**, *68*, 104272.

[7] Yu, A. F.; Jiang, P.; Lin Wang, Z. Nanogenerator as self-powered vibration sensor. *Nano Energy* **2012**, *1*, 418–423.

[8] Fan, F. R.; Tian, Z. Q.; Lin Wang, Z. Flexible triboelectric generator. *Nano Energy* **2012**, *1*, 328–334.

[9] Zi, Y. L.; Wang, J.; Wang, S. H.; Li, S. M.; Wen, Z.; Guo, H. Y.; Wang, Z. L. Effective energy storage from a triboelectric nanogenerator. *Nat. Commun.* **2016**, *7*, 10987.

[10] Zhu, G.; Peng, B.; Chen, J.; Jing, Q. S.; Wang, Z. L. Triboelectric nanogenerators as a new energy technology: From fundamentals, devices, to applications. *Nano Energy* **2015**, *14*, 126–138.

[11] Wang, Z. L. On Maxwell's displacement current for energy and sensors: The origin of nanogenerators. *Mater. Today* **2017**, *20*, 74–82.

[12] Yang, Z.; Yang, Y. Y.; Wang, H.; Liu, F.; Lu, Y. J.; Ji, L. H.; Wang, Z. L.; Cheng, J. Charge pumping for sliding-mode triboelectric nanogenerator with voltage stabilization and boosted current. *Adv. Energy Mater.* **2021**, *11*, 2101147.

[13] Wang, J. Y.; Pan, L.; Guo, H. Y.; Zhang, B. B.; Zhang, R. R.; Wu, Z. Y.; Wu, C. S.; Yang, L. J.; Liao, R. J.; Wang, Z. L. Rational structure optimized hybrid nanogenerator for highly efficient water wave energy harvesting. *Adv. Energy Mater.* **2019**, *9*, 1802892.

[14] Zhang, H.; Quan, L. W.; Chen, J. K.; Xu, C. K.; Zhang, C. H.; Dong, S. R.; Lü, C. F.; Luo, J. K. A general optimization approach for contact-separation triboelectric nanogenerator. *Nano Energy* **2019**, *56*, 700–707.

[15] Hao, C. C.; Wang, Z. K.; Cai, M. Z.; Liu, T. S.; Zhai, C.; Cui, J.; Zheng, Y. Q.; Xue, C. Y. High-performance coaxial reversal rotational triboelectric nanogenerator based on charge pumping strategy driving tip high voltage breakdown. *Nano Energy* **2024**, *128*, 109857.

[16] Bai, S. M.; Cui, J.; Zheng, Y. Q.; Li, G.; Liu, T. S.; Liu, Y. B.; Hao, C. C.; Xue, C. Y. Electromagnetic-triboelectric energy harvester based on vibration-to-rotation conversion for human motion energy exploitation. *Appl. Energy* **2023**, *329*, 120292.

[17] Wang, H.; Shi, M. Y.; Zhu, K.; Su, Z. M.; Cheng, X. L.; Song, Y.; Chen, X. X.; Liao, Z. Q.; Zhang, M.; Zhang, H. X. High performance triboelectric nanogenerators with aligned carbon nanotubes. *Nanoscale* **2016**, *8*, 18489–18494.

[18] Xu, J.; Zou, Y. J.; Nashalian, A.; Chen, J. Leverage surface chemistry for high-performance triboelectric nanogenerators. *Front. Chem.* **2020**, *8*, 577327.

[19] Wang, Z. K.; Hao, C. C.; Cai, M. Z.; Cui, J.; Zheng, Y. Q.; Xue, C. Y. A highoutput PDMS-MXene/gelatin triboelectric nanogenerator with the petal surface-microstructure. *Nano Res.* **2024**, *17*, 4151–4162.

[20] Wang, J.; Wu, C. S.; Dai, Y. J.; Zhao, Z. H.; Wang, A.; Zhang, T. J.; Wang, Z. L. Achieving ultrahigh triboelectric charge density for efficient energy harvesting. *Nat. Commun.* **2017**, *8*, 88.

[21] Wang, J.; Zhang, B. F.; Zhao, Z. H.; Gao, Y. K.; Liu, D.; Liu, X. R.; Yang, P. Y.; Guo, Z. T.; Wang, Z. L.; Wang, J. Boosting the charge density of triboelectric nanogenerator by suppressing air breakdown and dielectric charge leakage. *Adv. Energy Mater.* **2024**, *14*, 2303874.

[22] Lv, S. B.; Li, H. Y.; Xie, Y. Y.; Zhang, B. B.; Liu, B. C.; Yang, J.; Guo, H. Y.; Yang, Z. B.; Lin, Z. M. High-performance and durable rotational triboelectric nanogenerator leveraging soft-contact coplanar charge pumping strategy. *Adv. Energy Mater.* **2023**, *13*, 2301832.

[23] Feng, H. Q.; Bai, Y.; Qiao, L.; Li, Z.; Wang, E. G.; Chao, S. Y.; Qu, X. C.; Cao, Y.; Liu, Z.; Han, X. et al. An ultra-simple charge supplementary strategy for high performance rotary triboelectric nanogenerators. *Small* **2021**, *17*, 2101430.

[24] Xu, L.; Bu, T. Z.; Yang, X. D.; Zhang, C.; Wang, Z. L. Ultrahigh charge density realized by charge pumping at ambient conditions for triboelectric nanogenerators. *Nano Energy* **2018**, *49*, 625–633.

[25] Wang, H. M.; Xu, L.; Bai, Y.; Wang, Z. L. Pumping up the charge density of a triboelectric nanogenerator by charge-shuttling. *Nat. Commun.* **2020**, *11*, 4203.

[26] Wang, S. H.; Xie, Y. N.; Niu, S. M.; Lin, L.; Wang, Z. L. Freestanding triboelectric-layer-based nanogenerators for harvesting energy from a moving object or human motion in contact and non-contact modes. *Adv. Mater.* **2014**, *26*, 2818–2824.

[27] Lin, Z. M.; Zhang, B. B.; Xie, Y. Y.; Wu, Z. Y.; Yang, J.; Wang, Z. L. Elastic-connection and soft-contact triboelectric nanogenerator with superior durability and efficiency. *Adv. Funct. Mater.* **2021**, *31*, 2105237.

[28] Liu, T. S.; Cui, J.; Zheng, Y. Q.; Bai, S. M.; Hao, C. C.; Xue, C. Y. A self-powered inert-gas sensor based on gas ionization driven by a triboelectric nanogenerator. *Nano Energy* **2023**, *106*, 108083.

[29] Wang, R.; Cui, J.; Liu, Y. B.; Liu, D.; Du, C. H.; Yan, S. B.; Zheng, Y. Q.; Xue, C. Y. Multi-pulse triboelectric nanogenerator based on micro-gap corona discharge for enhancement of output performance. *Energy* **2022**, *244*, 122588.

[30] Zheng, Y. Q.; Liu, T. S.; Cui, J.; Zhang, Z. X.; Du, C. H.; Gao, X.; Chu, C. Q.; Xue, C. Y. High performance triboelectric nanogenerator with needle tips discharge for gas detection applications. *Sens. Actuators A: Phys.* **2023**, *362*, 114613.